

**PAPER**

# Sensitivity analysis and experimental evaluation of PID-like continuous sliding mode control

Michael Ruderman\*<sup>1</sup> | Johann Reger<sup>2</sup> | Benjamin Calmbach<sup>3</sup> | Leonid Fridman<sup>4</sup><sup>1</sup>University of Agder, P.B. 422, Kristiansand, 4604, Norway<sup>2</sup>Technische Universität Ilmenau, 98684 Ilmenau, Germany<sup>3</sup>Technische Universität Ilmenau, 98684 Ilmenau, Germany<sup>4</sup>Universidad Nacional Autónoma de México, 04510 Mexico City, Mexico**Correspondence**

\*Corresponding address. Email: michael.ruderman@uia.no

**Summary**

Continuous higher order sliding mode (CHOSM) controllers represent an efficient tool for disturbance rejection. For the systems with relative degree  $r$ , CHOSM approaches provide theoretically exact compensation of the matched Lipschitz perturbation, ensuring the finite-time convergence to the  $(r + 1)$ -th sliding-mode set, by using only information on the sliding output and its derivatives up to the order  $(r - 1)$ . In this paper, we investigate the disturbance rejection properties of a PID-like CHOSM controller, as the simplest and intuitively clear example which incorporates nonlinear actions on the output error, its derivative, and integration of its sign. We use the harmonic balance approach and develop an analysis of propagation of the matched Lipschitz perturbation through the control loop in frequency domain. The resulted solution appears in form of the Bode-like loci which depend also on the amplitude of harmonic disturbances. Such amplitude-frequency characteristics allow certain comparability with standard disturbance sensitivity functions of a linear PID-controlled system in frequency domain. Also a simple and straightforward design procedure for the robust linear PID controller targeting the second-order system plants under investigation is provided for benchmarking. Additional (parasitic) actuator dynamics, which can lead to self-induced steady oscillations, i.e. chattering, is ditto respected. A detailed experimental case study, accomplished on an electro-mechanical actuator in the laboratory setting, highlight and make the pros and cons of both PID and CHOSM controllers well comparable for a broadband disturbance rejection.

**KEYWORDS:**

Sliding mode control, harmonic balance analysis, disturbance rejection, sensitivity analysis, robust control design, higher order sliding mode

## 1 | INTRODUCTION

Sliding-mode controllers (SMC) are especially efficient for disturbance rejection[22]. The main disadvantage of SMC is the presence of the so-called chattering effect due to the discontinuity used in a control law, see e.g. [3],[4],[22]. Continuous higher order sliding mode (CHOSM) algorithms, see e.g. [10],[23],[15], [8],[9],[5],[13], [16],[19], are a class of homogeneous sliding mode controllers capable to compensate Lipschitz uncertainties and perturbations theoretically exactly, and generating a continuous control signal instead of a discontinuous one. These algorithms consist of a static homogeneous finite-time controller for

the nominal model of the system and a discontinuous integral action, aimed at estimating and compensating for the uncertainties and perturbations. CHOSM controllers can be seen as an extension of the (classical) super-twisting algorithm (STA) [10], ensuring the finite-time convergence to the  $(r + 1)$ -th sliding-mode set for systems with a relative degree  $r$ . CHOSM controllers are using only information on the sliding output and its derivatives up to the order  $(r - 1)$ . The homogeneity weight of the output variables in the CHOSM controllers is  $r + 1$ , cf. [15],[5],[13],[16], and it results, correspondingly, in a chattering amplitude of the order  $r + 1$  [12].

A PID-like continuous sliding mode controller introduced in [23], [5] is the simplest and intuitively clear CHOSM algorithm. For the systems with relative degree  $r = 2$ , it ensures the finite-time convergence to the third-order sliding-mode set using only information on the sliding output and its derivative. Moreover, when the actuator is fast enough, cf. [17], [18], the chattering effects caused by the discontinuity and discretization can be strongly attenuated. To generate the synthesis rules for PID-like controllers the authors of [19] used the harmonic balance method and made the PID-like controller gains adjusting the parameters of chattering. The latter is due to the presence of parasitic (actuator) dynamics. Finally, an approach proposed in [19] allows to minimize either the amplitude of chattering or the energy needed to maintain the system with relative degree two in a third-order sliding mode. The harmonic balance-based analysis of PID-like controllers opened the door for investigation of the propagation properties of CHOSM algorithms that will be used in this paper. The corresponding contribution of the paper is summarized as:

- an analysis of the PID-like CHOSM control based on its analytic describing function, allowing to estimate the disturbance sensitivity in frequency domain;
- a comparison of the steady-state properties of the CHOSM controller with a simple and straightforwardly designed robust linear PID controller, that is based on the upper bound of the disturbance sensitivity function;
- a detailed experimental case study, accomplished on an electro-mechanical actuator in the laboratory setting, highlighting and making the pros and cons of both PID and PID-like CHOSM controllers well illustrative.

The rest of the paper is organized as follows. In section 2, we address the PID-like CHOSM control [19]. First we introduce the control problem. Then, we summarize the CHOSM control with proportional, derivative and integral terms in a closed-loop configuration with external disturbances. Finally we perform the analysis based on harmonic balance and propagation of harmonic disturbances through the CHOSM-controlled system with additional parasitic actuator dynamics. Section 3 is devoted to a robust design of a linear PID control based on the sensitivity function. The comparative experimental case study is reported in detail in section 4. Brief conclusions are drawn by the end in section 5.

## 2 | PID-LIKE CONTINUOUS SLIDING MODE CONTROL

In this section, the class of dynamic systems under consideration is first stated together with the control problem. Then, the CHOSM [23, 5] targeted in this work is summarized for the reader convenience. Finally, the analysis based of harmonic balance equation and describing function of CHOSM control is developed, which allows consideration in frequency domain.

### 2.1 | Control problem

Consider the class of perturbed second-order systems which can be written, in time domain, as

$$\ddot{y}(t) = u(t) + d(t). \quad (1)$$

The single measurable system state is the output  $y(t)$ , and the available control channel is  $u(t)$ . The matched exogenous disturbance  $d(t)$  is assumed to be Lipschitz continuous, meaning  $|d/dt d(t)| \leq L$  while the upper bound  $L > 0$  is assumed to be known. Moreover, the control channel  $u$  can be subject to an additional first-order actuator dynamics with a unity gain and a not-negligible time constant  $\mu$ . In this case, which is also the one analyzed in section 2.3 and studied experimentally in section 4, the control channel will transform to

$$u(t) = v(t) - \mu \dot{u}(t), \quad (2)$$

where  $v(t)$  is the output value of a feedback controller is use. Note that if the actuator time constant can be neglected, i.e.  $\mu = 0$ , the system plant (1), (2) with the relative degree  $r = 3$  recovers to the one (1) with  $r = 2$ .

The targeted control problem is to analyze the residual stabilization control error  $y(t)$  is response to unbiased (i.e. zero mean-value) periodic disturbances with the known amplitude  $E$  and the upper bounded frequency range  $\omega < \omega_{\max}$ . A nonlinear feedback control which uses the output error, its time derivative, and integration is considered, while the standard PID linear feedback control is to be compared with it.

## 2.2 | CHOSM with proportional, derivative and integral terms

The CHOSM control, as a simplified version of the so-called Discontinuous Integral Controller [5, 16], is given by

$$v = -k_1 [y]^{1/3} - k_2 [\dot{y}]^{1/2} - k_3 \int \text{sign}(y) dt, \quad (3)$$

cf. [19, 23]. Here  $k_1, k_2, k_3 > 0$  are the properly designed control gains. It can be recognized that the corresponding three control terms are equivalent to the proportional, derivative, and integral feedback actions, respectively. The notation  $[x]^p \equiv |x|^p \text{sign}(x)$ , for a system variable  $x \in \mathbb{R}$  and a number  $0 \leq p \in \mathbb{R}$ , is a commonly used one, especially in the control related literature, so for example  $[x]^0 = \text{sign}(x)$ . The sign function is defined as

$$\text{sign}(x) = \begin{cases} 1, & \text{if } x > 0; \\ [-1, 1], & \text{if } x = 0; \\ -1, & \text{if } x < 0. \end{cases} \quad (4)$$

And the corresponding solutions  $y(t)$  are in the Filippov sense [6], meaning  $y(t)$  is a locally absolutely continuous function  $y : [0, T) \rightarrow \mathbb{R}$  for almost every  $t \in (0, T)$ .

For a perturbed second-order system, with the Lipschitz constant  $L > 0$  and the gains assignment  $k_1 = \lambda_1 L^{2/3}$ ,  $k_2 = \lambda_2 L^{1/2}$ , and  $k_3 = \lambda_3 L$  according to [19], ensures the finite-time convergence and insensibility of (1) with respect to the matched disturbances  $d(t)$ , cf. with Fig. 1. This is, however, under assumption of no additional actuator dynamics  $D(j\omega)$ . Further recall that the scaling factors  $\lambda_1, \lambda_2, \lambda_3 > 0$  can be assigned so as to ensure the finite-time stability of (1) with the known  $L$ , cf. [19] and section 2.3 below.

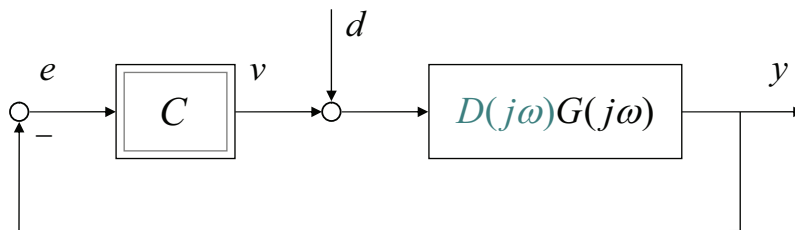


**FIGURE 1** Standard single-input-single-output (SISO) feedback control loop with the objective of disturbance rejection.

Note that in Fig. 1, a generic notation of the feedback control  $C$  refers to a transfer function  $v(j\omega)/e(j\omega)$  in case of the linear PID-control, and to a continuous mapping  $e \in \mathbb{R} \mapsto v \in \mathbb{R}$  in case of the nonlinear CHOSM control. The linear part of the system plant (1) is denoted by  $G(j\omega)$ , respectively.

## 2.3 | Harmonic balance based analysis

One of the remarkable features of the nonlinear CHOSM control (3), that can be used for analyzing the loop propagation of harmonic signals, is the closed analytic form of the describing function (DF), as provided in [18]

$$N(A, \omega) = \frac{2\alpha_1 k_1}{\pi A^{2/3}} + j \frac{2\alpha_2 k_2 \omega^{1/2}}{\pi A^{1/2}} + \left( \frac{4k_3}{\pi A} \right) \left( \frac{1}{j\omega} \right). \quad (5)$$

Here  $\alpha_1 \approx 1.821$  and  $\alpha_2 \approx 1.748$  are the coefficients of the first harmonic approximation [19]. Obviously,  $j$  denotes the imaginary unit of the complex argument. Since the DF method is based upon the filtering hypothesis, cf. [2], it is imperative to assume

that the CHOSM control will operate on a plant which has low-pass characteristics. This is fulfilled for the linear process  $D(j\omega)G(j\omega)$ , cf. Fig. 1, where

$$D(s) = (\mu s + 1)^{-1}.$$

Then, the propagated harmonic in  $y(t)$ , and so in  $e(t)$ , allows to compare the closed-loop characteristics including (5) with those of a linear feedback controller  $C(s)$ , both at steady-state.

Since the CHOSM control (3) provides a finite-time convergence for the  $d$ -perturbed double integrator plant, cf. Fig. 1, an additional actuator behavior in the loop, cf. (2), can deteriorate convergence and induce residual steady-state oscillations, also known as chattering. The transfer properties of such servo system, i.e. from  $d$  to  $y$ , can be analyzed provided the external signal  $d(t)$  is slow in comparison with the self-excited oscillations. Then, the input can be assumed approximately constant on one period of the fast oscillations, cf. [4].

Here it is worth recalling that the fast self-excited oscillations of the CHOSM controlled output can be preestimated as for the corresponding amplitude and frequency, [19]:

$$\tilde{A} = L \left( \frac{2\alpha_1 \lambda_1}{\pi \mathbb{K}^2 (1 - \mathbb{K}^2)} \right)^{3/2} \mu^3 \quad \text{and} \quad \Omega = \frac{\mathbb{K}}{\mu}. \quad (6)$$

That means the CHOSM controlled closed-loop system with  $d = 0$  and actuator dynamics parameterized by  $\mu$ , cf. (2), will experience (after convergence) the residual steady-state oscillations with frequency  $\Omega$  and amplitude  $\tilde{A}$ . The parameter  $\mathbb{K} \in (0, 1)$  is the solution of the nonlinear equation, cf. [19],

$$2\mathbb{K}\lambda_1^{3/2} - (1 - \mathbb{K}^2)^{3/4} \lambda_2 \lambda_1^{3/4} + (1 - \mathbb{K}^2)^{3/2} \lambda_3 = 0. \quad (7)$$

The closed-loop system (Fig. 1) with the CHOSM control can be analyzed as two separate dynamic subsystems interacting with each other via a set of parameters: the results of the solution of the "fast" subsystem are used by the "slow" subsystem [4]. This decomposition is possible if the external input, i.e.  $d(t)$ , is much slower than the self-excited oscillations, that is normally the case. That means for the preestimated self-oscillations (6) one needs to guarantee  $\omega_{\max} \ll \Omega$ .

For analyzing propagation of an external disturbance

$$d(t) = E \sin(\omega t + \phi_e) \quad (8)$$

through the closed control loop (Fig. 1), we are to solve the corresponding harmonic balance equation

$$\frac{1}{W(j\omega)} + N(A, \omega) = \frac{E}{A} e^{j(\phi_e - \phi)}, \quad (9)$$

which applies under the above separation assumption of the fast (i.e. chattering) and slow (i.e. disturbance driven) system dynamics. Here  $W(j\omega)$  is the transfer function of the overall linear system plant, including the actuator dynamics, and  $\phi$  is the output phase lag of steady-state oscillations at  $\omega$ .

In the following, for the sake of simplicity and without loss of generality, we assume a zero-phase unity disturbance, meaning  $E = 1$  and  $\phi_e = 0$ . Note that for other  $0 < E \neq 1$ , another  $A(\omega)$ -solutions of (9) need to be determined each time, thus making the residual steady-state oscillations in  $y(t)$  both the frequency- and amplitude-dependent, i.e.  $A(\omega, E)$ . We also assume an actuator-perturbed linear plant given by

$$W(j\omega) = \frac{K}{j\omega(j\omega\tau + 1)(j\omega\mu + 1)}, \quad (10)$$

where an additional first-order time delay element with the time constant  $\tau$  and input gain  $K$  appears instead of the free integrator, cf. (1), (2). Notice that the plant transfer function (10) coincides with that of the experimental system investigated in this study, cf. further with sections 3, 4. For obtaining  $A = A(\omega)$ , we take first the absolute value

$$\left| \frac{1}{W(j\omega)} + N(A, \omega) \right|^2 = \frac{1}{A^2}. \quad (11)$$

Then, substituting (10) and (5) into (11), one obtains the solution of  $A$  in dependency of  $\omega$ , and that for each given set of the numerical parameter values.

For the assigned  $L = 0.4$ , the determined system parameters  $K = 0.0408$ ,  $\tau = 0.0067$ ,  $\mu = 0.0012$  (cf. section 4), and the CHOSM control parameters  $\lambda_1 = 2.7$ ,  $\lambda_2 = 5.345$ ,  $\lambda_3 = 1.1$ , which minimize the oscillations amplitude [19], the  $A = A(\omega)$

solution is exemplarily obtained by solving the equation

$$A^{-2} = \left( \frac{1.69}{A^{2/3}} - 0.19 \omega^2 \right)^2 + \left( 24.5 \omega (1 - 8.02 \cdot 10^{-6} \omega^2) + \frac{3.76 \sqrt{\omega}}{\sqrt{A}} - \frac{0.56}{A \omega} \right)^2, \quad (12)$$

which results from (11) with (10) and (5). Note that the otherwise unknown upper bound  $L$  was tuned based on the numerical simulations and experiments, so that the residual oscillations of the output  $y(t)$  at steady-state are acceptably low. Numerical solution of (12) obtained by means of the Maple software yields the results visualized for in Fig. 2, while the numerical solutions for  $E = 10$  are equally depicted for the sake of comparison.

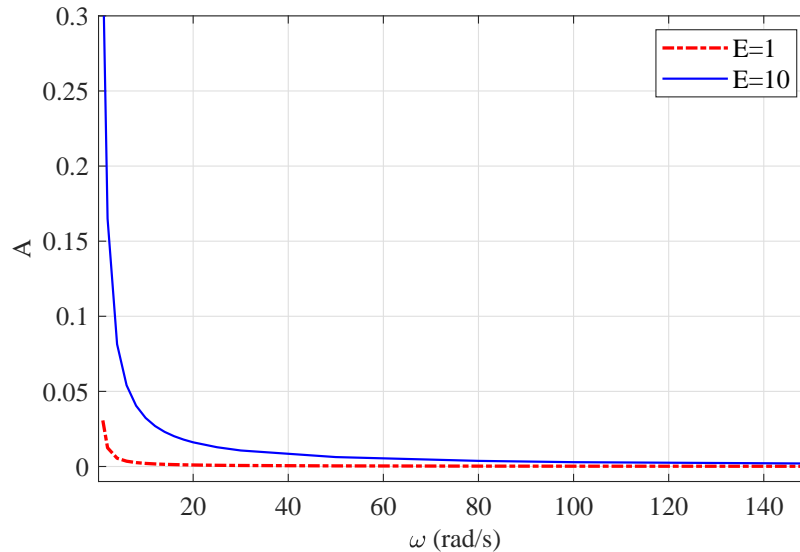


**FIGURE 2** Computed, based on (12), amplitude  $A$  of the output steady-state oscillations over the angular frequency  $\omega$  of the periodic disturbance, with  $E = 1$  (dash-dotted red line) and  $E = 10$  (solid blue line).

### 3 | ROBUST LINEAR PID CONTROL

In this section, we provide a two-step procedure for robust PID control design, which is resting on an underlying PD control with the stable pole-zero cancellation and upper bound of the disturbance sensitivity function.

In order to reduce the design complexity of a linear PID controller and, correspondingly, to limit the degrees-of-freedom during the parameters tuning, a stable pole-zero cancellation is first performed. Then, the tuning parameters reduce to only one overall control gain and one integration time constant. To this end, applying the underlying PD controller

$$C_{PD}(s) = \gamma(\tau s + 1), \quad (13)$$

with the proportional gain  $\gamma > 0$  and derivative time constant  $\tau > 0$ , the dominant pole of the plant  $\bar{G}(s)$  at  $p = -1/\tau$  is canceled. Note that the performed linear control design assumes the reduced plant model

$$\bar{G}(s) = \frac{K}{s(\tau s + 1)}, \quad (14)$$

cf. (10), while taking into account  $\mu \ll \tau$ . Worth noting is that any small  $\mu > 0$  will still create an additional yet faster pole of the linear system plant and, thus, inherently affect the resulting closed-loop dynamics. However, this is minor for the proposed design which is based on the sensitivity function, as becomes obvious from the developments shown below. Following to that, only the  $\gamma$ -gain is used for further PD control synthesis.

Since the disturbance rejection is of our major interest, the input disturbance sensitivity function

$$S_{yd}(s) = \frac{\bar{G}(s)}{1 + \bar{G}(s)C(s)} \quad (15)$$

is considered. Applying the PD controller (13) results in

$$S_{yd,PD}(j\omega) = \frac{-K}{(\omega\tau - j)(\omega - jK\gamma)}, \quad (16)$$

with the corresponding magnitude response

$$\left| S_{yd,PD}(j\omega) \right| = \frac{K}{\sqrt{\omega^2\tau^2 + 1}\sqrt{\omega^2 + K^2\gamma^2}}. \quad (17)$$

Note that it has its maximum at steady-state, i.e.

$$\left| S_{yd,PD}(j\omega) \right|_{\omega=0} = \frac{1}{\gamma} > \left| S_{yd,PD}(j\omega) \right| \quad \forall \omega > 0, \quad (18)$$

which is equivalent to

$$\left\| S_{yd,PD} \right\|_{\infty} = \frac{1}{\gamma}. \quad (19)$$

Therefore, for a given worst-case amplification of the matched disturbance, the proportional gain  $\gamma$  is chosen as its inverse.

Next, in order to ensure the steady-state accuracy, we make use of a PID controller

$$C_{PID}(s) = \frac{\gamma(\tau s + 1)(T_1 s + 1)}{T_1 s}, \quad (20)$$

with the integration time constant  $T_1$  to be the second tuning parameter. This leads to the corresponding sensitivity function  $S_{yd,PID}$ , cf. (15), with the magnitude characteristics

$$\left| S_{yd,PID}(j\omega) \right| = \frac{KT_1\omega}{\sqrt{(K\gamma - T_1\omega)^2 + (KT_1\gamma\omega)^2}\sqrt{\tau^2\omega^2 + 1}}. \quad (21)$$

In order to utilize the previous considerations (i.e. of  $S_{yd,PD}$ ), we show that (21) is bounded by  $\left\| S_{yd,PD} \right\|_{\infty}$ , i.e. that

$$\left| S_{yd,PID}(j\omega) \right| \leq \frac{1}{\gamma} \quad \forall \omega > 0 \quad (22)$$

holds true. This can be seen by considering

$$\begin{aligned} \left| S_{yd,PID}(j\omega) \right|^2 &= \frac{(KT_1\omega)^2}{\left[ (K\gamma - T_1\omega)^2 + (KT_1\gamma\omega)^2 \right] \underbrace{(\tau^2\omega^2 + 1)}_{>1 \forall \omega, \tau > 0}} \\ &\leq \frac{(KT_1\omega)^2}{(K\gamma - T_1\omega)^2 + (KT_1\gamma\omega)^2} \equiv \Theta(j\omega) \end{aligned}$$

and knowing that  $K, T_1, \omega > 0$ , which yields

$$\Theta(j\omega) = \frac{1}{\left( \frac{K\gamma - T_1\omega}{KT_1\omega} \right)^2 + \gamma^2} \leq \frac{1}{\gamma^2}.$$

Therefore, the relation (22) becomes evident and can be used for determining an appropriate proportional gain, that for a specified minimal attenuation of the input disturbance. The conservativeness of such design is discussed below in section 4.4, that for the resulted system plant and  $\gamma$  value.

The next free tuning parameter  $T_1$  is chosen based on the frequency characteristics of the open-loop and the predefined phase margin  $\Phi$ . The open-loop transfer function (with zero initial conditions) is given by

$$H(s) = C_{PID}(s)\bar{G}(s) = \frac{K\gamma(T_1 s + 1)}{T_1 s^2}, \quad (23)$$

and consists of a double-integrator and one stable zero. Therefore, the corresponding phase never crosses  $-180^\circ$ , leading to a (theoretically) infinite gain margin. However, the phase margin  $\Phi$  can be used as a further robustness measure, especially with respect to an additional phase lag. Here we recall that the plant transfer function  $\bar{G}(s)$  does not take into account an additional higher-frequent actuator dynamics.

Consider the amplitude and phase at the open-loop crossover frequency  $\omega_s$  given by

$$|H(j\omega_s)| = 1 \quad (24a)$$

$$\pi + \arg(H(j\omega_s)) = \Phi. \quad (24b)$$

From (23), it can be seen that

$$H(j\omega) = \frac{-K\gamma(1 + jT_1\omega)}{T_1\omega^2} = -\frac{K\gamma}{T_1\omega^2} - j\frac{K\gamma}{\omega}.$$

Hence, at  $\omega_s$  one obtains

$$|H(j\omega_s)| = \frac{K\gamma\sqrt{1 + \omega_s^2 T_1^2}}{\omega_s^2 T_1} \quad \text{and} \quad (25a)$$

$$\arg(H(j\omega_s)) = \arctan(T_1\omega_s) - \pi, \quad T_1, \omega_s > 0. \quad (25b)$$

The combination of (24) and (25) yields

$$\omega_s = \frac{K\gamma\sqrt{1 + \tan^2(\Phi)}}{\tan(\Phi)} \quad \text{and} \quad (26a)$$

$$T_1 = \frac{\tan(\Phi)}{\omega_s}. \quad (26b)$$

The above shown developments result in a two-step procedure for the robust PID control design:

1. Set a worst-case disturbance amplification  $S_{\max}$  which is then leading to

$$\gamma = \frac{1}{S_{\max}}. \quad (27)$$

2. Set the desired phase margin  $\Phi$  and calculate

$$T_1 = \frac{\tan^2(\Phi)}{K\gamma\sqrt{1 + \tan^2(\Phi)}}. \quad (28)$$

With the system and design parameters  $\tau, \gamma, T_1$ , the PID controller (20) is then entirely determined.

## 4 | EXPERIMENTAL CASE STUDY

### 4.1 | System Setup

The second-order system under investigation is an electro-mechanical linear-displacement actuator depicted in Fig. 3. The induced relative motion is indirectly measured by the contactless inductive displacement sensor with a nominal repeatability of  $\pm 12$  micrometers. Despite all mechanical elements are rigid, and the system dynamics is inherently of the second-order, while having one free integrator, the nominal electrical time constant  $\mu = 1.2$  msec of the voice-coil-motor is not fully negligible. Furthermore, it is justified that the system has a relatively high level of the sensor and process noise. The former is due to a contactless sensing, while the latter is due to additional parasitic by-effects which are not captured by the simplified linear modeling, cf. sections 3 and 4.2. The real-time control board operates the system with the set sampling rate of 5 kHz. Further details on the experimental system can be found in e.g. [21]. The partially available and partially identified system parameters are given below.

### 4.2 | Modeled and Identified System Plant

The second-order dynamics of the system plant under consideration is assumed to be represented by

$$m\ddot{y}(t) + \sigma\dot{y}(t) = \frac{\Psi}{R}v(t) - mg, \quad (29)$$

with input  $v(t)$  (in volts, V) and output  $y(t)$  (in meters, m). The values of the moving mass  $m$ , electromotive force constant  $\Psi$ , and coil resistance  $R$  are given by

$$m = 0.538 \text{ kg}, \quad \Psi = 17.16 \frac{\text{Vs}}{\text{m}}, \quad R = 5.32 \frac{\text{V}}{\text{A}} \quad (30)$$

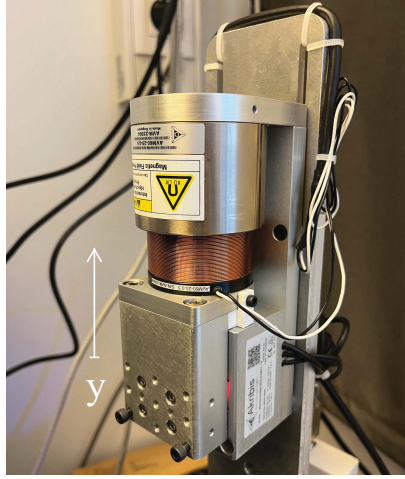


FIGURE 3 Experimental setup of the motion system.

and originate from the weight measurement and the actuator data sheet [1]. Note that the gravitational force  $F_g = -mg$  with the gravity constant  $g = 9.81 \text{ ms}^{-2}$  can be directly compensated with  $v_g = mgR\Psi^{-1}$  and is, therefore, not a part of further discussions. In order to estimate the unknown damping parameter  $\sigma > 0$ , we apply  $v + v_g$  leading to

$$\frac{m}{\sigma} \ddot{y}(t) + \dot{y}(t) = \frac{\Psi}{R\sigma} v(t). \quad (31)$$

Using the Laplace transform, with zero initial conditions, the transfer function of the system plant reads

$$\bar{G}(s) = \frac{K}{s(\tau s + 1)} \quad \text{with} \quad K = \frac{\Psi}{R\sigma}, \quad \tau = \frac{m}{\sigma}. \quad (32)$$

Due to a free integrative behavior and bounded displacement  $y \in [0, 18]$  mm, the identification experiments are conducted in a closed-loop, as in Fig. 1. In order to minimize the noise amplification and not exciting further dynamics, a pure proportional controller with a relatively low feedback gain  $\gamma = 100$  is utilized here for the parameters identification. Starting from the middle of the displacement range, at steady-state  $y_0 = 9$  mm, a sinusoidal input disturbance

$$d(t) = E \sin(\omega_d t) \quad (33)$$

is applied to  $v(t)$  for exciting the closed-loop system. The amplitude  $E \in [0.7, 1.5]$  V is chosen to ensure a sufficient excitation without input- and state-saturation, in accord with the frequency range  $\omega_d \in [1, 1000]$  rad/s. A measurement of 20 periods at steady-state is utilized for the frequency response estimation at each frequency. With use of the auto-correlation  $R_{uu}(\cdot)$  and cross-correlation functions  $R_{uy}(\cdot)$ , the magnitude and phase at  $\omega_d$  can be calculated as, cf. with e.g. [7],

$$\left| \bar{G}(j\omega_d) \right| = \frac{R_{uy,\max}}{R_{uu}(0)} \quad \text{and} \quad \angle \bar{G}(j\omega_d) = -\omega_d \Delta\tau, \quad (34)$$

where  $\Delta\tau$  is the time lag between two correlation functions. The resulting Bode plot of the experimentally collected frequency-response data is depicted in Fig. 4. The phase at low frequencies corresponds to the integrating behavior. However, high frequencies show an increasing time delay, in terms of a phase lag, which is not covered by the second-order model (32). Therefore, only the magnitude response is used for the transfer function estimation. The least-squares optimal fit, by using  $\left| \bar{G}(j\omega_d) \right|$  with  $\omega_d \in [4, 380]$  rad/s, results in  $\sigma = 80.49$ . This yields the remaining parameter values

$$K = 0.0408 \quad \text{and} \quad \tau = 6.684 \text{ ms.}$$

The Bode plot of the estimated  $\bar{G}(j\omega)$  is also depicted in Fig. 4 over the measurements.

### 4.3 | Robust Exact Differentiator

In order to use the (otherwise) unavailable output derivative  $\dot{y}(t)$ , we apply a robust exact differentiator [11] (further as RED), which is based on the sliding-mode estimation, see e.g. [22] for basics. Its remarkable features are the insensitivity to a bounded



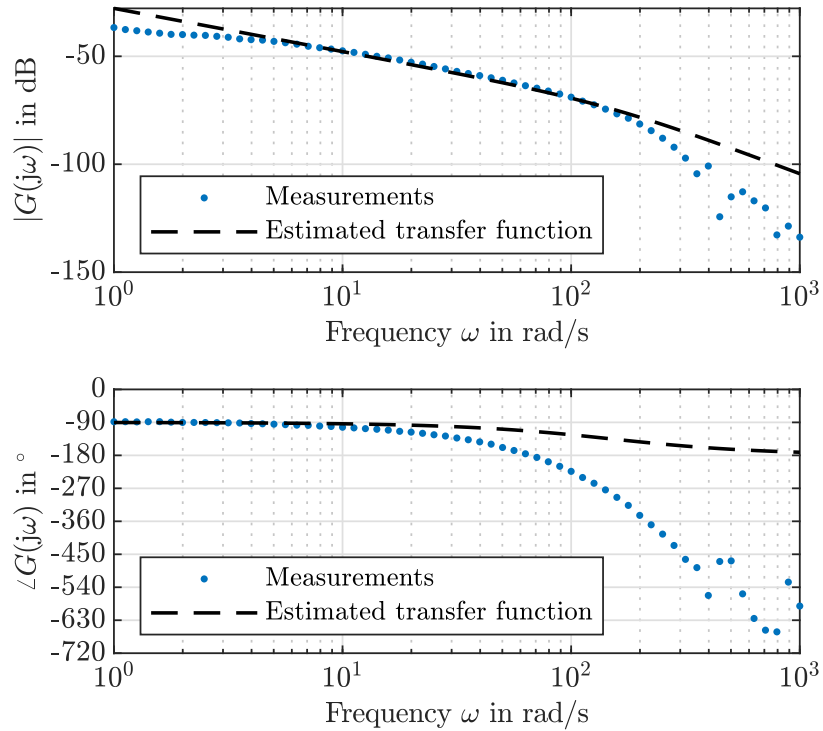


**FIGURE 4** Bode plot of the experimental data and estimated transfer function.

noise, provided the Lipschitz constant of n-th time-derivative is available, and the finite-time convergence. This makes a RED (theoretically) free of a phase lag. Recall that the latter is, otherwise, deteriorating the closed-loop performance in case of a low-pass filtering of the differentiated measurement of  $y(t)$ . The second-order RED, cf. [14], with the parametrization according to [20], is given by

$$\dot{x}_0 = x_1 + 3.1 r \left| y - x_0 \right|^{\frac{2}{3}} \text{sign}(y - x_0), \tag{35a}$$

$$\dot{x}_1 = x_2 + 3.2 r^2 \left| y - x_0 \right|^{\frac{1}{3}} \text{sign}(y - x_0), \tag{35b}$$

$$\dot{x}_2 = 1.1 r^3 \text{sign}(y - x_0), \tag{35c}$$

where the scaling factor  $r > 0$  is the single design parameter. It is worth noting that  $r^{n+1}$  (here  $r^3$ ) corresponds to the Lipschitz constant  $L$  of the highest derivative  $y^{(n)}$ , cf. [20]. The second-order RED provides  $x_0(t) = y(t)$ ,  $x_1(t) = \dot{y}(t)$ ,  $x_2(t) = \ddot{y}(t)$ , for all  $t > t_c$ , where  $t_c$  is the convergence time. Also we note that the second-order (and not first-order) RED is purposefully used here, in order to obtain a smoother estimate  $x_1(t)$  of the output derivative. The scaling factor  $r = 8$  was experimentally tuned on the collected  $y(t)$  data, for which an up-chirp signal until  $\omega = 80$  rad/s disclosed a still satisfying match between the  $x_1(t)$  estimate and the theoretically calculated  $\dot{y}(t)$ .

An exemplary experimental evaluation of the RED (35) with  $r = 8$  is shown in Fig. 5, in comparison with the discrete time derivative of the measured signal  $y(t)$  which is then low-pass filtered with a cutoff frequency of 100 Hz.

#### 4.4 | Synthesized PID controller

The design approach developed in section 3 is used to determine the PID controller for the identified plant  $\bar{G}$ . For a sufficient disturbance rejection and robustness, we choose

$$S_{\max} = -52 \text{ dB} \quad \text{and} \quad \Phi = 60^\circ,$$

leading to

$$\gamma = 400 \quad \text{and} \quad T_1 = 0.092 \text{ s.} \tag{36}$$

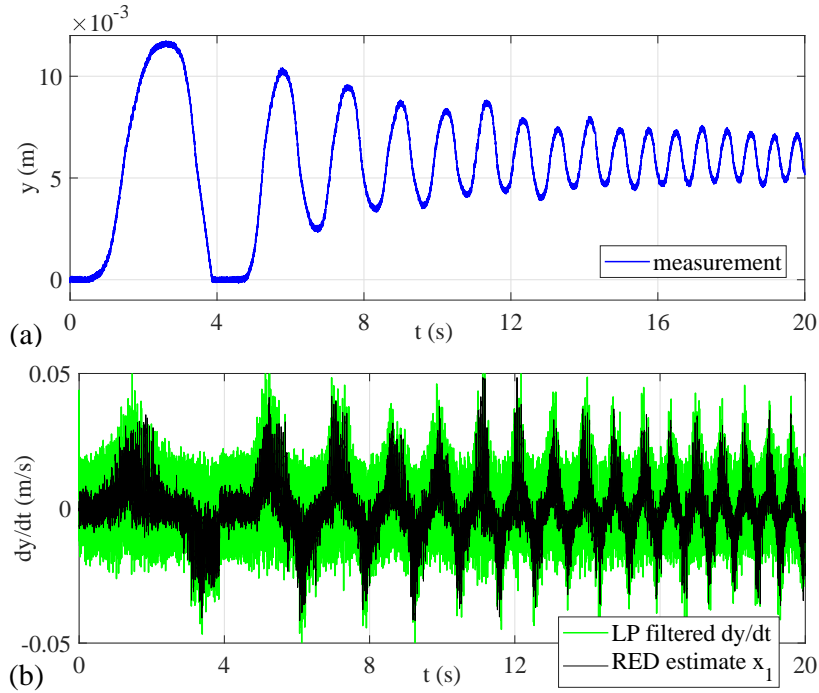


**FIGURE 5** Exemplary evaluation of the 2nd order RED with  $r = 8$ : the measured output value in (a) and RED estimate  $x_1$  over the low-pass (LP) filtered discrete time derivative of  $y$  in (b).

The magnitude plot of  $S_{y_d}$ , when using the underlying PD controller, is depicted in Fig. 6 opposite to the use of PID controller, that for a large variation of the integration time constant  $T_1$ . Obviously, the maximum disturbance amplification is only little dependent on the value of  $T_1$ , while a clear asymptotic reduction for lower frequencies is evident. The PID controller with  $T_1 = 0.1$  s, cf. with the determined parameters (36), provides certain optimality in shaping the disturbance sensitivity function. It yields without sharp peak of  $|S_{y_d}|$  and without a flat plateau of  $|S_{y_d}| \rightarrow S_{\max}$  upper bound which is dictated by the underlying PD control. A closer look at the H-inf norms for a variation of  $T_1$  in the relevant range, see Fig. 7, confirms (19) and (22). Worth

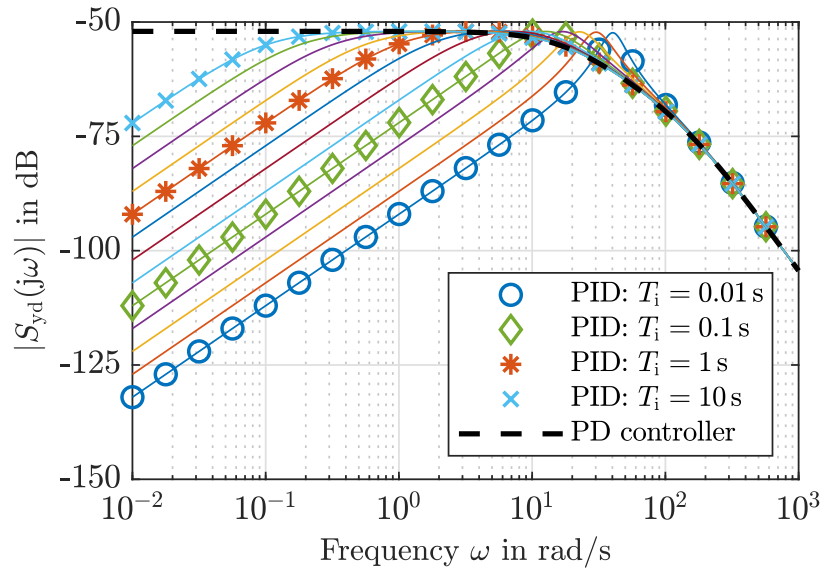


**FIGURE 6** Magnitude plot of the input disturbance sensitivity function when using the PD controller opposite to PID controllers with the different integration time constants  $T_1 \in [0.01, 10]$  rad/s.

noting here is that for this set of parameters, the above mentioned conservativeness of (22) is limited to 0.31 dB.

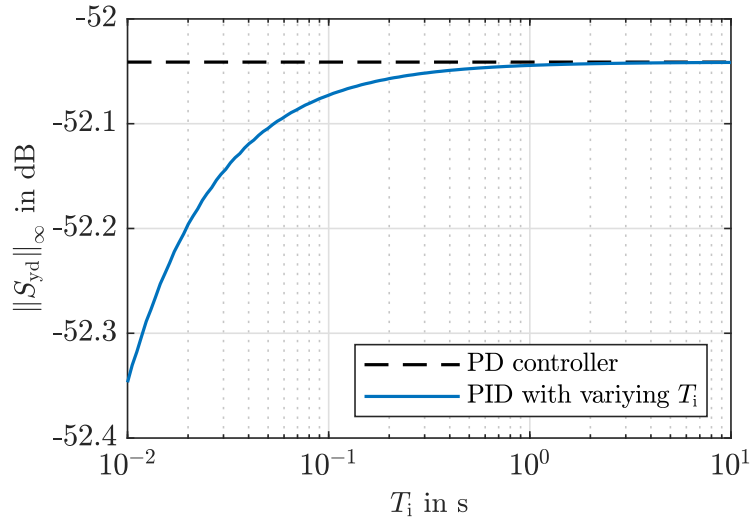


FIGURE 7 H-inf norms of the disturbance sensitivity functions from Fig. 6.

For ease of implementation and a better comparison with the PID-like sliding-mode controller, the parallel form of PID controller  $C_{\text{PID}}$  (20) reads as

$$\bar{C}_{\text{PID}}(s) = K_p + K_I \frac{1}{s} + K_D s. \quad (37)$$

The proportional, integral, and derivative gains are

$$K_p = \gamma \frac{T_I + \tau}{T_I} = 429.064, \quad (38)$$

$$K_I = \frac{\gamma}{T_I} = 4348.267, \quad (39)$$

$$K_D = \gamma \tau = 2.674, \quad (40)$$

respectively. Note that the parameters result directly from comparison of the coefficients between  $C_{\text{PID}}$  and  $\bar{C}_{\text{PID}}$ .

In order to evaluate efficiency of the proposed PID design, as well as the accuracy of the model fit and the associated linear loop shaping, cf. section 4.2, the sinusoidal input disturbance  $d(t)$ , given by (33), is used in experiments. The assigned amplitude is  $E = 1$  V and the frequencies selected exemplary closer to  $\omega_{\text{max}}$  are

$$\omega_{d,1} = 5 \frac{\text{rad}}{\text{s}}, \quad \omega_{d,2} = 10 \frac{\text{rad}}{\text{s}} \quad \text{and} \quad \omega_{d,3} = 20 \frac{\text{rad}}{\text{s}}.$$

The experimental results are depicted in Fig. 8 by disclosing the control error  $e = y - y_0$ . Evaluating the theoretically expected disturbance attenuation at  $\omega_{d,1,\dots,3}$  i.e.  $|\tilde{S}_{yd}(j\omega_{d,1,\dots,3})| = \{-58.6, -52.9, -53.8\}$  dB and comparing these values with the corresponding numbers calculated out from the experiments  $\{-57.5, -52.6, -50.1\}$  dB, see Fig. 8, one can recognize a good accordance between both.

#### 4.5 | Bode-like Loci of PID and CHOSM control

The frequency domain analysis of the disturbance sensitivity characteristics at steady-state, developed in section 3 for the linear PID-controlled and in section 2.3 for the nonlinear CHOSM-controlled closed-loop systems, yield both comparable in terms of the Bode-like loci. Note that in case of the CHOSM-controlled closed-loop system one can consider only the Bode-like characteristics, correspondingly diagrams, since the harmonic output response is not only frequency- but also disturbance amplitude-dependent, i.e.  $A(\omega, E)$ . Moreover, the available solution of (11), allows regarding the amplitude but not phase response, that is however sufficient for analysis and comparison of the residual output errors. The amplitude response of the  $d$ -to- $y$  characteristics is compared in Fig. 9 for the PID-controlled closed-loop sensitivity function and CHOSM-controlled

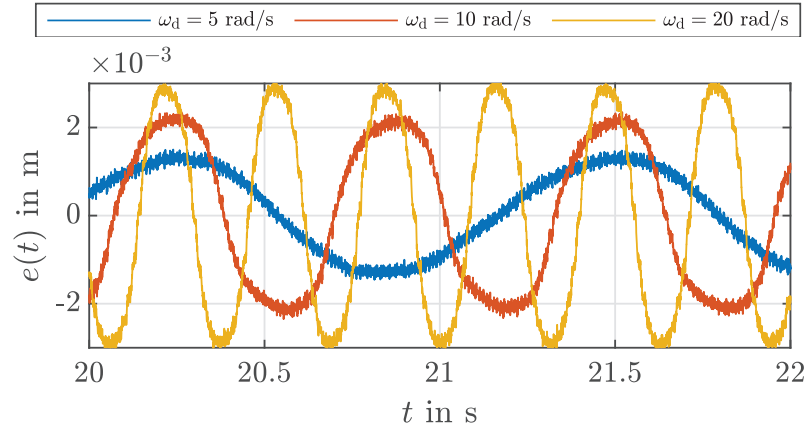


**FIGURE 8** Measured control error  $e$  of  $\tilde{C}_{\text{PID}}$  for the disturbance attenuation.

closed-loop harmonic balance equation. The disturbance amplitude  $E = 1$ , the same as evaluated below in experiments, is assumed for the loci depicted in (a), and amplitude  $E = 10$  for the loci depicted in (b). One can recognize an advantage of

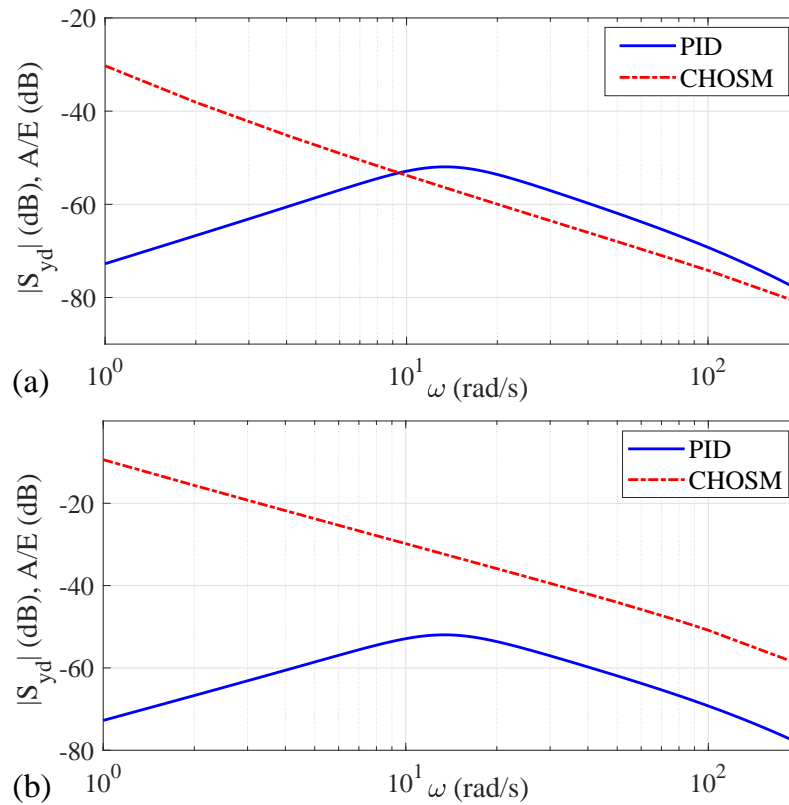


**FIGURE 9** Amplitude response of  $d$ -to- $y$  frequency characteristics, for PID-controlled loop sensitivity function (21), and CHOSM-controlled harmonic balance (11): for the disturbance amplitude  $E = 1$  in (a) and  $E = 10$  in (b).

the continuously decreasing  $E$  to  $A$  ratio of CHOSM with an increasing disturbance frequency, cf. Fig. 2. On the contrary, the sensitivity function of the PID-controlled closed-loop shows a typical increase with a peak, first after which the disturbance to output ratio starts to decrease as well.

#### 4.6 | Controllers Comparison for Broadband Disturbances

The design CHOSM and PID controllers, cf. sections 2 and 3, are evaluated experimentally and compared to each other for the disturbance rejection. The applied disturbance value constitutes an up-chirp signal

$$d(t) = E \sin((\omega_0 + \alpha t)t) \quad (41)$$

with a linearly increasing frequency, i.e.  $\alpha > 0$ , and the start and end frequencies at 0.06 rad/s and 30 rad/s, correspondingly. Note that the preestimated frequency of the fast oscillations, see (6), (7), is  $\Omega = 587$  rad/s, and thus the requirement of  $\omega_{\max} = 30 \ll \Omega$  is well fulfilled. The chirp amplitude is  $E = 1$  V. The selected runtime of 65 s ensures that the transient, correspondingly convergence, phase of the control response is passed at already lower frequencies, cf. Fig. 10 (a). Note that the convergence phase, even though finite-time, is relatively long for the CHOSM control, that for the range of feasible gain values. Following to that, a steady-state disturbance rejection behavior can be compared for the time frame about  $t > 10$  s. It can be seen that the

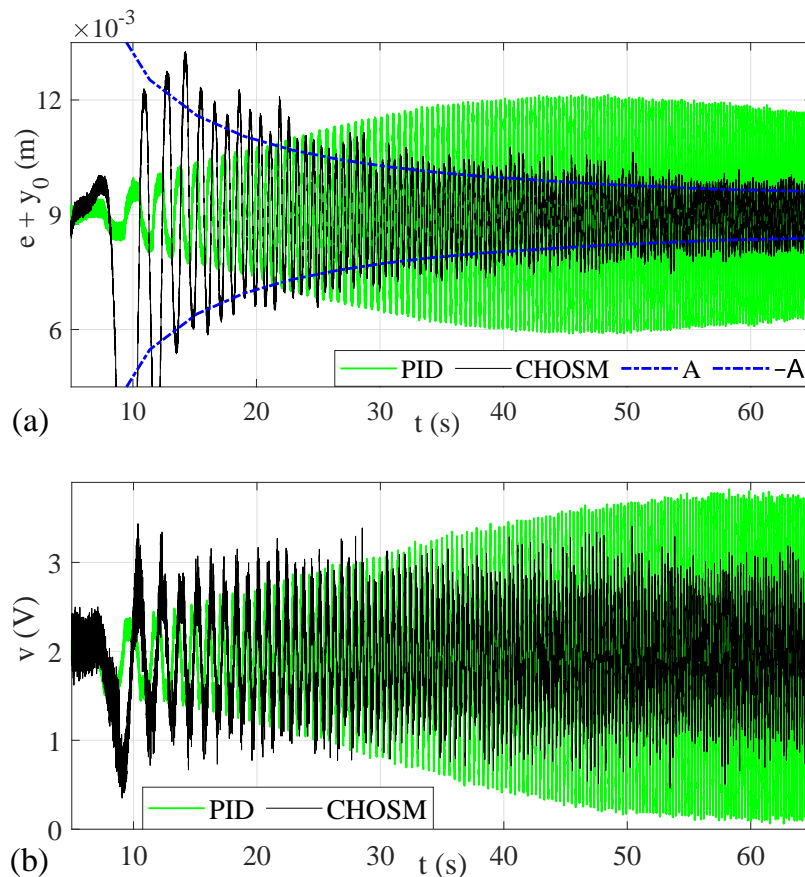


**FIGURE 10** Experimental results of the PID and CHOSM controllers on rejection of the up-chirp disturbance with bandwidth 0.06–30 rad/s: the control error (around the reference position  $y_0 = 9$  mm) in (a) and control signal in (b)

error pattern of the PID control follows the expected shape of the disturbance sensitivity function, cf. Fig. 6. On the contrary, the CHOSM control error is continuously decreasing with an increasing frequency, that corresponds to the CHOSM sensitivity function, cf. section 4.5. The envelope  $A(\omega)$ , obtained by means of solving the harmonic balance equation (11) and equally plotted in Fig. 10 (a), fits very exactly with the measured  $y(t)$ , which argues in favor of the developed harmonic balance based analysis.

The period where the control error of both PID and CHOSM controllers are approximately the same, i.e. at the time about 24 s, corresponds to the disturbance frequency  $\omega_d \approx 9.5$  rad/s. Starting from that, the CHOSM control performs superior comparing

to the PID one in compensating for higher frequency disturbances, that is well in accord with frequency characteristics shown in Fig. 9 (a).

Regarding the control values, see Fig. 10 (b), one can recognize that for the PID control, the signal pattern is also inline with the frequency response of the closed-loop system (cf. Fig. 1). Here, the transfer characteristics between  $d(j\omega)$  and  $v(j\omega)$  are indicative and can be directly computed based on the transfer functions  $\bar{G}(s)$  and  $\bar{C}(s)$ . One can recognize that with an increasing angular frequency, the amplitude of the PID control value  $v(t)$  is also growing, thus resulting in a higher power and, correspondingly, energy consumption. On the contrary, the control value of the CHOSM compensator keeps an almost constant amplitude level, that speaks for a lower power consumption. Also recall that for finite-time convergence of CHOSM controller, the control signal tends to opposite value of the perturbation, that is the case for chirp disturbance of a constant amplitude, cf. Fig. 10 (b).

The comparison between the simulated and experimental response of the closed loop with the CHOSM controller is further exemplary shown in Fig. 11. Here the same experimental data, a higher-frequency clipping from Fig. 10, is used. Note that in the numerical simulation of the system (29), augmented by the disturbance (41) and control (3), an additional band-limited white noise is added to the output  $y(t)$ , so as to bring the behavior of the modeled control system closer to the real one. Up to the noise level, the simulated and experimental responses of the CHOSM-controlled output coincide well with each other, see Fig. 11.

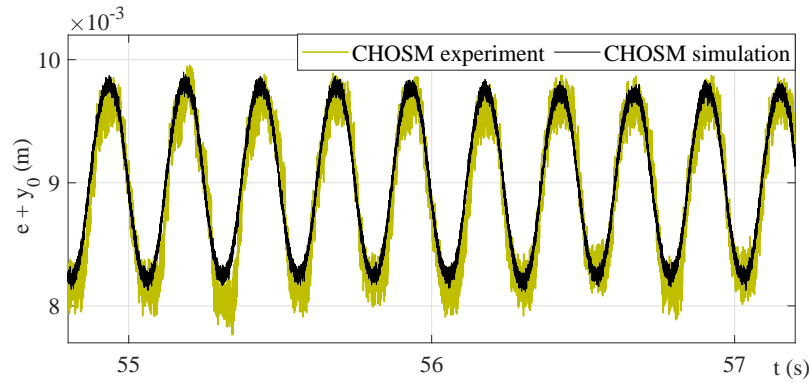


**FIGURE 11** Comparison between the simulated and experimental response of CHOSM control; experimental data are from higher-frequencies from Fig. 10.

## 5 | CONCLUSIONS

A PID-like continuous higher order sliding mode (CHOSM) controller, known to be robust for rejection of the matched Lipschitz continuous perturbations, was analyzed in terms of a disturbance sensitivity function. Such frequency-domain approach, which takes additionally into account the amplitude of steady-state harmonics of the CHOSM control loop (also when perturbed by an actuator) allows a comparison with standard linear feedback controllers. Due to the structural similarity, i.e. with feedback of the output, its derivative and integral, the CHOSM control can and has been compared to a standard linear PID one, designed also for rejection of the matched disturbances. Both controllers were evaluated experimentally as the fair competitors. The developed two-step procedure for a robust PID controller design yields *two tunable parameters*, the overall control gain and the integration time constant. Both are shown associated with the H-infinity norm of the disturbance sensitivity function and with the desired phase margin, respectively. The CHOSM control parametrization follows exactly the analysis and developments provided in [19], yielding only *one tunable parameter*, which is the scaling factor out from the Lipschitz constant of perturbations. The comparative study of both controllers is made for the second-order experimental motion system with an additional (fast) parasitic dynamics of the actuator. The two-parameters linear model of the system plant is identified in frequency domain and shown to be sufficient for designing the feedback controllers. For the time derivative of the output, required for both PID and CHOSM control schemes, the robust second-order sliding-mode differentiator is used in experiments. The PID and CHOSM controllers

are evaluated experimentally on rejection of a broadband matched disturbance, which is an up-chirp between 0.06 rad/s and 30 rad/s.

The resulted control performance is shown to be fully inline with the theoretically expected (i) disturbance sensitivity characteristics (i.e. sensitivity function) of the PID control loop, and (ii) describing-function based prediction of the steady-state harmonic oscillations of the CHOSM control loop. The disturbance rejection performance of the CHOSM control is shown to be clearly decreasing with an increasing frequency, as for the control error pattern, and more energy efficient as for the control signal amplitude. At the same time, the transient behavior of the CHOSM control disclosed inferior comparing to the PID one, that for the maximal achievable  $L$ -scaling factor of the CHOSM control parametrization. The  $L$ -scaling factor, also related to the actuator dynamics, proved to be most sensitive for application of the CHOSM control. In summary, the demonstrated practical comparison of PID and CHOSM controllers allows a better understanding and distinction of the application benefits and challenges of their use, when compensating for the amplitude- and band-specific disturbances.

## ACKNOWLEDGMENTS

This work was financially supported by DAAD scholarship programme: Research Stays for University Academics and Scientists (DAAD ref. no. 91893483). Fourth author is acknowledging support by CONACyT (Consejo Nacional de Ciencia y Tecnologia) project 282013, PAPIIT-UNAM (Programa de Apoyo a Proyectos de Investigacion e Innovacion Tecnologica) IN 115419.

## References

- [1] Akribis, *Voice coil motor user manual*, 2018. URL <https://www.akribis-sys.de/en/>.
- [2] D. Atherton, *Nonlinear Control Engineering - Describing Function Analysis and Design*, Workingam Beks, 1975.
- [3] I. Boiko, *Frequency-domain analysis of fast and slow motions in sliding modes*, Asian Journal of Control **5** (2003), no. 4, 445–453.
- [4] I. Boiko, *Oscillations and transfer properties of relay servo systems - the locus of a perturbed relay system approach*, Automatica **41** (2005), no. 4, 677–683.
- [5] E. Cruz-Zavala and J. A. Moreno, *Higher order sliding mode control using discontinuous integral action*, IEEE Transactions on Automatic Control **65** (2019), no. 10, 4316–4323.
- [6] A. Filippov, *Differential Equations with Discontinuous Right-hand Sides*, Dordrecht: Kluwer Academic Publishers, 1988.
- [7] R. Isermann and M. Münchhof, *Identification of dynamic systems: an introduction with applications*, Springer, 2011.
- [8] S. Kamal et al., *Continuous terminal sliding-mode controller*, Automatica **69** (2016), 308–314.
- [9] S. Laghrouche, M. Harmouche, and Y. Chitour, *Higher order super-twisting for perturbed chains of integrators*, IEEE Transactions on Automatic Control **62** (2017), no. 7, 3588–3593.
- [10] A. Levant, *Sliding order and sliding accuracy in sliding mode control*, International journal of control **58** (1993), no. 6, 1247–1263.
- [11] A. Levant, *Robust exact differentiation via sliding mode technique*, Automatica **34** (1998), no. 3, 379–384.
- [12] A. Levant, *Chattering analysis*, IEEE Transactions on Automatic Control **55** (2010), no. 6, 1380–1389.
- [13] A. Mercado-Uribe and J. A. Moreno, *Discontinuous integral action for arbitrary relative degree in sliding-mode control*, Automatica **118** (2020), 109018.
- [14] J. A. Moreno, *Lyapunov function for Levant's second order differentiator*, IEEE 51st conference on decision and control (CDC).

- [15] J. A. Moreno, *Discontinuous integral control for mechanical systems*, *IEEE 14th International Workshop on Variable Structure Systems (VSS)*, 142–147.
- [16] J. A. Moreno, E. Cruz-Zavala, and Á. Mercado-Urbe, *Discontinuous integral control for systems with arbitrary relative degree*, *Variable-Structure Systems and Sliding-Mode Control*, 2020. 29–69.
- [17] U. Pérez-Ventura and L. Fridman, *Design of super-twisting control gains: A describing function based methodology*, *Automatica* **99** (2019), 175–180.
- [18] U. Pérez-Ventura and L. Fridman, *When is it reasonable to implement the discontinuous sliding-mode controllers instead of the continuous ones? frequency domain criteria*, *International Journal of Robust and Nonlinear Control* **29** (2019), no. 3, 810–828.
- [19] U. Pérez-Ventura, J. Mendoza-Avila, and L. Fridman, *Design of a proportional integral derivative-like continuous sliding mode controller*, *International Journal of Robust and Nonlinear Control* **31** (2021), no. 9, 3439–3454.
- [20] M. Reichhartinger et al., *A robust exact differentiator toolbox for Matlab®/Simulink®*, *IFAC-PapersOnLine* **50** (2017), no. 1, 1711–1716.
- [21] M. Ruderman, *Motion control with optimal nonlinear damping: from theory to experiment*, *Control Engineering Practice* **127** (2022), 105310.
- [22] Y. Shtessel et al., *Sliding mode control and observation*, Springer, 2014.
- [23] C. A. Zamora, J. A. Moreno, and S. Kamal, *Control integral discontinuo para sistemas mecánicos*, *2013 Congreso Nacional de Control Automático (CNCA AMCA)*, 11–16.

